COMMUNICATION

Directly Deposited Quantum Dot Solids Using a Colloidally Stable Nanoparticle Ink

Armin Fischer, Lisa Rollny, Jun Pan, Graham H. Carey, Susanna M. Thon, Sjoerd Hoogland, Oleksandr Voznyy, David Zhitomirsky, Jin Young Kim, Osman M. Bakr,* and Edward H. Sargent*

The solution-phase chemistry of infrared-emitting colloidal quantum dots (CQDs) has attracted much attention thanks to the utility of these materials in both biological[1,2] and optoelectronic[3–5] applications. PbS CQDs, for example, are of interest in solar applications owing to their small bandgap and large Bohr exciton radius, which together allow bandgap tuning over the full solar spectral range.[4] Among other third-generation photovoltaics, such as copper indium gallium selenide (CIGS)[5,6] and copper zinc tin sulfide (CZTS),[7,8] colloidal quantum dots specifically offer the opportunity to create tandem or multi-junction solar cells on the basis of the same material, because of its widely tunable bandgap. The solution processability of CQD materials could in principle enable highly scalable and flexible manufacturing processes to be developed, such as roll-to-roll processing.

Advances in CQD photovoltaics have recently resulted in solar cell power conversion efficiencies exceeding 7%.[9–11] Although these performance levels are promising, all high-performing device results to date have relied on a multiple layer-by-layer strategy for film fabrication (**Figure 1**a) rather than a single-layer deposition process. The layer-by-layer approaches use a solid-state exchange of the long aliphatic ligands, typically required in and after synthesis for colloidal stability; shorter linkers are necessary for film densification and conduction.

This solid-state exchange process suffers the dual drawbacks of low efficiency in the utilization of quantum dots—typically below 1%—combined with incompatibility with roll-to-roll processing. An ideal fabrication process would instead be lossless from a materials utilization perspective and would allow fast, serial, large-area deposition of an electronic-transport-compatible film.

In this work, we develop a semiconductor ink with the goal of enabling large areas of solar cell substrates to be coated in a single deposition step, thereby eliminating tens of deposition steps necessary with the previous layer-by-layer method. We sought an approach that would achieve highly efficient utilization of CQD materials (Figure 1b). While the layer-by-layer, solid-state treatment approach previously published provides less than 0.1% yield in its application of CQD materials from their solution phase onto the substrate (Figure 1a), the new approach developed herein achieves nearly 100% use of available CQDs (Figure 1b).

Our approach relies on creating a colloidal dispersion based on small, transport-compatible ligands. Since the final CQDs to be used in film fabrication are thus available in solution, forming the final film simply involves removing the solvent via drying. We prove that we are able to preserve passivation of nanoparticle surfaces in these liquids. By contrast, prior CQD photovoltaic device works have relied on steric effects to maintain colloidal stability and have required solid-state removal of bulky ligands, such as oleic acid (OA).

We began by investigating whether previously published routes to short-ligand-stabilized solutions[12,13] could meet the requirements for CQD photovoltaics. These have relied on water as solvent. Unfortunately, we found that the photoluminescence quantum efficiency (PLQE) of our CQD solution decreased from 50% for the as-synthesized OA-capped nanoaparticles in toluene, down to 10% in the aqueous solution (**Figure 2**a). The results are consistent with the concern that the alkaline additives required in published routes act as photoluminescence quenchers:[14–17] indeed, hydroxides are known antagonists to PbS CQD surface quality.[18]

We used analytical ultracentrifugation (Figure 2b) to study the quality of the aqueous colloidal dispersion.[19] A well-dispersed colloid based on ≈3 nm nanoparticles (physical diameter) was expected to exhibit a ≈5 nm hydrodynamic diameter in solution. Instead, Figure 2b shows a broad hydrodynamic diameter distribution spanning many tens of nanometers, providing evidence of severe agglomeration. Furthermore, we observed appreciable precipitation of nanocrystal material beginning immediately after redispersion with complete precipitation occurring within 24 hours.

We therefore investigated novel avenues for solution-phase exchange and redispersion with the goal of maintaining high PLQE, which would indicate preservation of passivation, and prioritizing colloidal stability. In addition, we sought an approach that would produce a final dispersion consisting of

Dr. A. Fischer,[+] L. Rollny,[+] G. H. Carey,
Dr. S. M. Thon, Dr. S. Hoogland, Dr. O. Voznyy,
D. Zhitomirsky, Dr. J. Y. Kim, Prof. E. H. Sargent
Department of Electrical and Computer Engineering
University of Toronto
10 King's College Road, Toronto, Ontario
M5S 3G4, Canada
E-mail: ted.sargent@utoronto.ca
Dr. J. Pan,[+] Prof. O. M. Bakr
Materials Science and Engineering
King Abdullah University of Science and Technology
Thuwal 23955–6900, Saudi Arabia
E-mail: osman.bakr@kaust.edu.sa
[+]A.F., L.R., and J.P. contributed equally to this work.
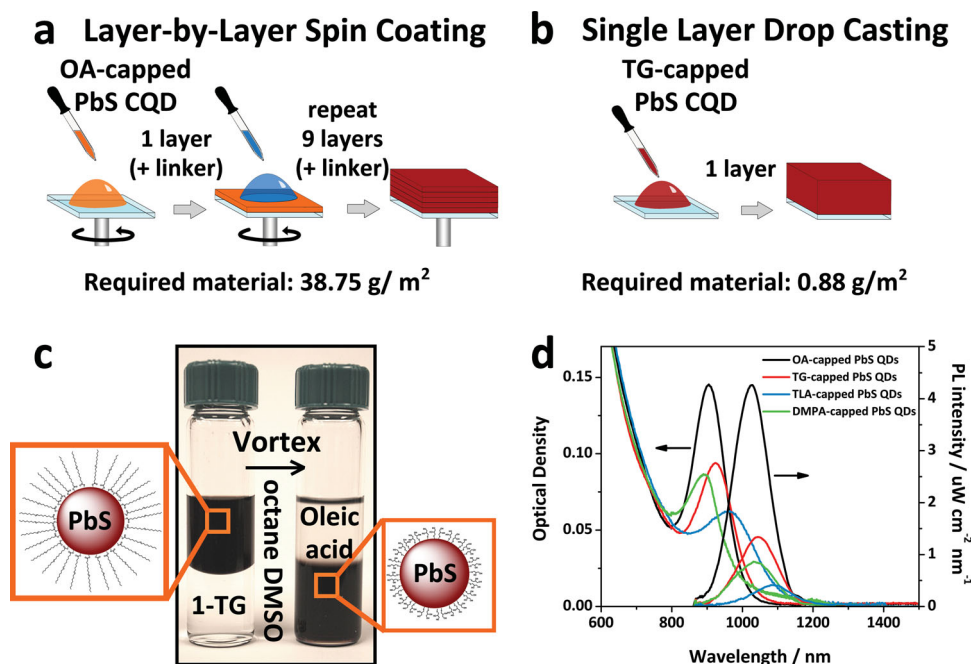
Figure 1. a) Schematic of the standard layer-by-layer spin-coating process with active materials usage yield and required total material indicated. b) Photograph of the as-synthesized long-ligand-capped PbS CQD solution before the solution exchange (left) and the exchanged short-ligand-capped CQD solution in a non-polar solvent (right). c) Schematic of the single-step film process with active materials usage yield and required total material indicated. d) absorbance and photoluminescence quantum efficiency measurements displaying versatility of the process using small hyrdophilic mercaptans.

CQDs and the desired final ligand alone, requiring no additives or other excess stabilizers.

We posited that small hydrophilic mercaptans (≤C3) could potentially be paired with a well-matched polar solvent with these goals in mind. We used a single-step exchange process to transfer the oleic acid (OA)-capped nanoparticles to the new phase; the substitution reaction happened as the particles crossed the phase boundary.[12,13] Owing to the high affinity of the thiol group for the metal cation sites on the CQD surfaces, the OA ligand is efficiently displaced by the thiol-terminated ligand. In successful exchanges, we observed a clear octane phase following the exchange, leading us to conclude that the transfer of the PbS CQDs across phases occurred with very high yield. We found that the best processes yielded the same results when carried out in air or inert conditions and that the ultimate solutions were colloidally stable over several weeks.

Ultimately, we came to rely on dimethyl sulfoxide (DMSO) as the solvent both for exchange and for final redispersion: even though we tested several polar solvent systems, including dimethylformamide and formamide, only DMSO resulted in a colloidally stable solution. Similarly, we explored the small hydrophilic mercaptans 1-thioglycerol (TG), thiolactic acid (TLA), and dimercaptopropionic acid (DMPA), monodentate mercaptane ligands did not lead to stable colloids after the exchange. Here we found that the exchange based on TG, which is known to be an effective stabilizing agent for pH-adjusted aqueous solutions,[14–17] led to the best combination of quantum efficiency and colloidal stability (Figure 1d) among the investigated ligands.

We sought to characterize the resultant CQD inks for suitability as photovoltaic materials. Figure 2a shows the absorption and photoluminescence spectra, which are measures of preservation of quantum confinement and of the extent of retention of quantum dot passivation, following the exchange with TG redispersed in different solvents.

The as-synthesized CQDs show quantum confinement with a well-defined excitonic peak near 900 nm, close to the optimum single-junction solar cell bandgap. The excitonic peak for the TG-capped PbS CQDs was substantially preserved following the ligand exchange. The redispersion into DMSO resulted in a slight red shift of both the emission and absorption peaks compared to the as-synthesized CQDs. The red shift may be explainable via extension of the electron–hole pair wavefunction into the thiol ligands, leading to a modest decrease in the CQD bandgap that we expected from simulations.

We measured the PL quantum yield of PbS CQDs capped with TG in DMSO versus in water. PLQE is an indicator of the degree of surface passivation of CQDs. The as-synthesized PbS CQDs display a PLQE of 50% and a peak emission wavelength of 1025 nm (≈1.21 eV). We observed a dramatic loss in PLQE for the unstable aqueous solution and only a modest loss to 24% for the DMSO redispersion, which provides evidence for substantial preservation of CQD passivation, although suggests that there is room for further optimization of the process.

We used analytical ultracentrifugation to study further the quality of the dispersion in these nanoparticle inks. In contrast to the aqueous case, CQD samples dispersed in DMSO showed a narrow size distribution with a hydrodynamic diameter in the range of 5 nm (Figure 2b). Considering the relatively high

COMMUNICATION
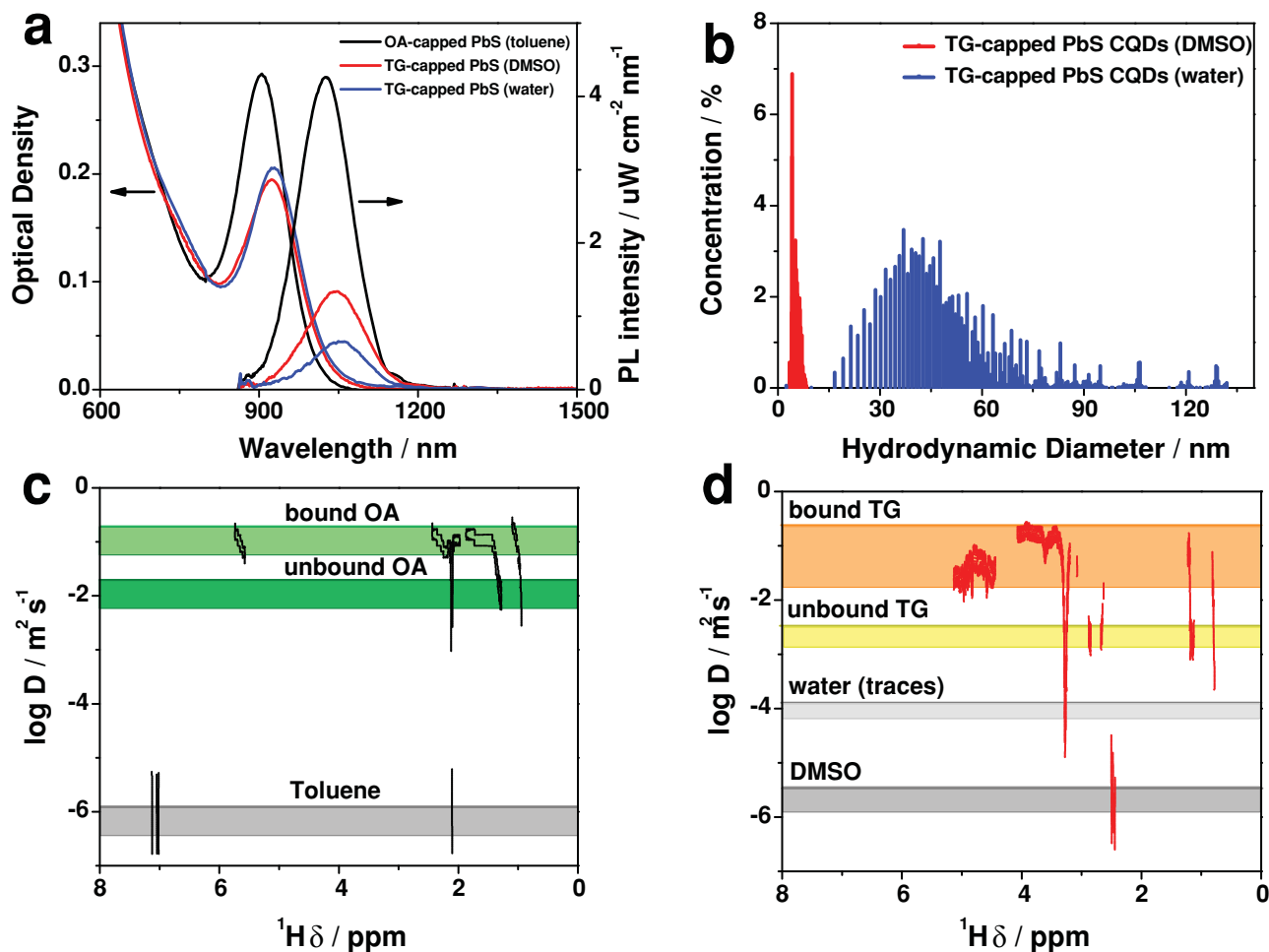
Figure 2. Characterization of OA-capped PbS CQDs in toluene (black), TG-capped PbS CQDs in DMSO (red) and TG-capped PbS CQDs in water (blue) by a) absorbance and photoluminescence quantum efficiency measurements displaying preserved quantum confinement and quenched photoluminescence after the ligand exchange. b) Analytical ultracentrifugation illustrating superior monodispersity of the TG-capped CQDs in DMSO. c) Diffusion-ordered spectroscopy (DOSY) NMR spectroscopy of OA-capped CQD before. d) After the exchange to TG; elucidating the binding modes of different ligand species in solution to the CQD surface and the underlying stabilization mechanisms.

PLQE, narrow particle distribution, and sustained quantum confinement for TG-capped CQDs in DMSO, our ensuing investigations focused on this system.

We used diffusion-ordered spectroscopy (DOSY) ^{1}H NMR[20] to elucidate the stabilization mechanism of CQDs in solution. The determination of the diffusion coefficients of the species present in the CQD solutions facilitates the extrapolation of their binding modes to the CQD surface.[21,22] The 2D spectra are plotted in Figure 2c,d.

For OA-capped PbS CQDs (Figure 2c), NMR indicated signatures consistent with the presence of OA bound to the PbS CQD surface and unbound OA interacting with the bound species, both as expected. The detailed analysis shows a fingerprint signature of bound OA at a low diffusion constant of $\approx 1 \times 10^{-10}$ m^2 s^{-1} evidenced by a broadened NMR signal. The ^{1}H NMR signal at 5.34 ppm corresponds to the double bond of oleic acid at C9. The region from 2.3 to 1.2 ppm shows the typical CH$_2$ signal of an aliphatic chain, and the sharpness of the CH$_3$ signal at 0.879 ppm indicates the presence of less

rigidly bound molecules. At a slightly increased diffusion constant of around 2×10^{-10} m^2 s^{-1}, sharper NMR signals for CH$_2$ and CH$_3$ point to a loosely bound diffuse double layer of OA molecules. The presence of only one signal for the OA double bond suggests that the double bonds of bound and unbound oleic acid overlap via π–π stacking; this can contribute to the steric stabilization of the OA-capped CQDs. The sharp peaks at a high diffusion constant ($\approx 6 \times 10^{-10}$ m^2 s^{-1}) with the ^{1}H NMR signatures of 2.34 ppm and 7.38–7.00 ppm are related to the toluene-dispersing solvent.

After ligand exchange, complete removal of oleic acid in the TG-capped CQDs in DMSO solution (Figure 2d) was proven by the absence of the C=C double bond signatures at 5.34 ppm in the ^{1}H NMR spectrum. DOSY further reveals a termination of the PbS CQD surfaces with TG, indicated by the presence of two OH species. The spectra also suggest the presence of small amounts of unbound TG, evidenced by the presence of free SH groups at higher diffusion coeffcients. We hypothesize that the unbound ligand helps to stabilize OH-terminated PbS
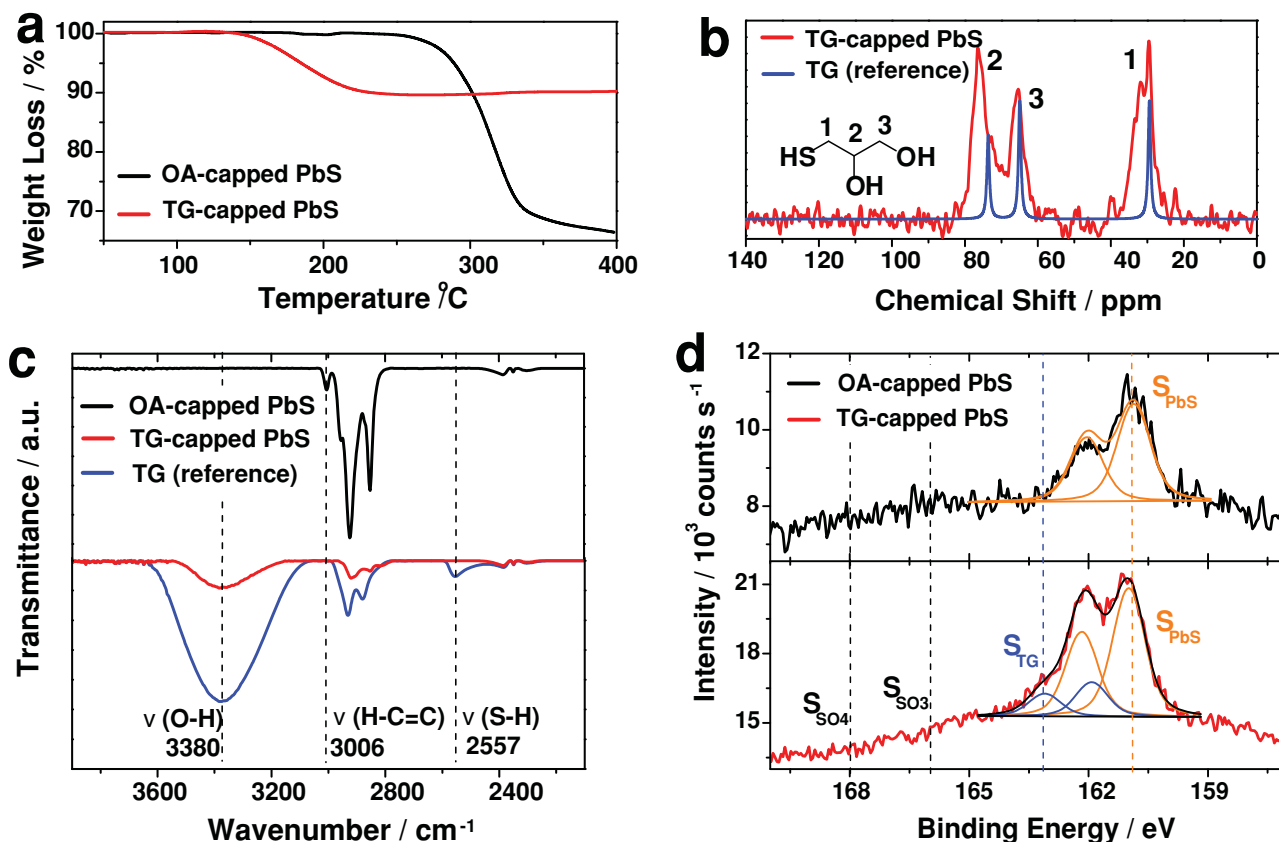
Figure 3. Characterization of the film properties of OA-capped (black) and TG-capped PbS CQDs (red) and TG as a reference (blue) via a) thermogravimetric analysis to document weight loss before and after the ligand exchange. b) Fourier transformation infrared spectroscopy to illustrate the completeness of the ligand exchange. c) ^{13}C solid-state NMR spectroscopy to show the absence of unbound TG in the films. d) X-ray photoelectron spectroscopy to verify the high quality of the CQD materials displaying no oxidized species.

CQD surfaces via hydrogen bonding (vide infra). This finding emphasizes the importance of using a polar solvent to stabilize CQDs capped with a short, polydentate ligand, such as TG.

The absence of an S–H signal in the NMR spectra at very small diffusion constants indicates that TG is bound via the sulfur moiety to the CQD surface. This is also reinforced from the fact that the broad ^{1}H NMR signals for CH$_2$ at 3.49 to 2.45 ppm and OH at 4.84 and 4.61 ppm occur at small diffusion constants of around 0.75×10^{-10} and 1.5×10^{-10} m^2 s^{-1}, respectively. Additionally, sharper peaks with similar diffusion constants of 3.0×10^{-10} m^2 s^{-1} indicate the presence of unbound TG ligand with a sharp S–H signal at around 1.1 to 0.9 ppm.

We propose that a stabilizing interaction via hydrogen bonding is suggested by the similarity of the diffusion constants of the trace amounts of unbound TG and the bound ligands. This view is supported by zeta potential measurements that show that a weak value of –7 mV for TG-capped CQDs in DMSO (Figure S1, Supporting Information), excluding electrostatic interactions playing a leading role in the colloidal stability of this system. The interaction of DMSO with carbohydrates via hydroxyl-groups monitored by NMR has been previously reported.[23] DMSO is highly polarizable and should therefore stabilize the CQDs efficiently.

These results paint a picture of DMSO, providing a highly polarizable solvent environment, yet one that is free from protic attack, and not relying on solvent additives, allowing it to facilitate the formation of a device-compatible ready-to-use CQD ink without the requirement of additives to adjust the solution pH.[14–17]

We carried out quantitative and qualitative solid-state analyses of device-compatible films made using our CQD inks via a single-step deposition method carried out in an inert environment. Our substrate consisted of a TiO$_2$ electrode deposited on a fluorine-doped tin oxide (FTO) coated glass slide. Oxygen plasma treatment of the substrate prior to solution deposition enhanced the wettability of the surface and led to a homogenous and pinhole-free TG-capped PbS CQD film as seen in SEM (Figure S2, Supporting Information). To analyze the material composition in detail, we performed thermogravimetric analysis (TGA) of the drop-cast TG and OA-capped films. Our measurements (**Figure 3**a) reconfirmed the complete removal of oleic acid during the solution-phase ligand exchange, which was consistent with DOSY NMR. The removal of organic matter in the OA-capped PbS CQD films occurred at 350 °C, as evidenced in the weight loss of 35% seen in the TGA trace of Figure 3a. By contrast, the loss of organic matter from the TG-capped PbS films happened at a lower temperature (150 °C) in

a single weight loss step, again reconfirming that oleic acid had been removed completely prior to redispersion. In addition, the overall reduction in weight loss percentage was decreased owing to the lower molecular weight of the shorter ligand.

We used FTIR spectroscopy to reconfirm that our TG-capped CQDs were free from OA and were OH-terminated (Figure 3b). The exchange of OA-capped PbS CQDs to TG results in OH-terminated CQD surfaces, indicated by the presence of the OH-stretching vibrations at 3380 cm^{-1}. The absence of the distinct thiol stretch at 2557 cm^{-1} (which would signal unbound mercaptans) indicates that any excess of TG that had been present in the solution-phase is removed by washing prior to film deposition.[24,25] Finally, the absence of the C=C stretching vibration strictly assigned to the double bond of oleic acid[26] from the TG-capped sample clearly shows that the solution exchange process leads to OA-free quantum dot films.

These findings are confirmed by ^{13}C cross-polarization magic angle spinning (CP-MAS) NMR measurements on TG-capped PbS CQD films, as shown in Figure 3c. The broadening of the peaks indicates that all detectable TG present in the films is bound to the PbS CQD surfaces.

Oxidized species can act as recombination centers in semiconductor materials and are known to degrade CQD photovoltaic device performance.[27] We used X-ray photoelectron spectroscopy (XPS) measurements to search for signatures of oxidation in our films. The measurements (Figure 3d) indicated that our TG-capped PbS quantum dots are free of trap-state forming oxidized sulphur species (if present, the signal owing to oxidized sulphur species would occur in the range of 166–169 eV). As expected, a single additional sulphur species signal at 162 eV in the TG-capped PbS CQD film XPS spectrum indicates that TG is bound to the PbS CQD surfaces via the carbon-thiol moiety.[27]

As a proof of concept, we made a CQD solar cell by a single-step deposition. We simply dried our stable CQD inks atop a TiO$_2$ electrode. This allowed us to achieve nearly complete materials utilization. This represents a 1000-fold better utilization of materials than the existing spin-coating followed by crosslinking layer-by-layer process (Figure 1a,b).

The device used the depleted heterojunction architecture[28] in which the TiO$_2$ film serves as the n-type semiconductor. As can be seen in the transmission electron microscopy image in **Figure 4**a (inset), the drop-casting process resulted in a smooth, homogeneous CQD film (Figure 4b, inset) with a thickness of 200 nm. The top contacts consisted of 30 nm of thermally evaporated MoO$_3$, 50 nm of electron beam evaporated Au and 120 nm of thermally evaporated Ag.

We measured the current–voltage characteristics (Figure 4a) in an inert nitrogen environment under 100 mW cm^{-2} simulated AM1.5G illumination, an external quantum efficiency (EQE) spectrum of an average device, and the film absorbance (Figure 4b) of TG-capped PbS CQD devices. Our champion device exhibited solar power conversion efficiency (PCE) of 2.1% with an open circuit voltage of 0.51 V, a short circuit current density of 9.2 mA cm^{-2}, and a fill factor of 35%. While the efficiency leaves room for further improvement, it is the highest CQD solar efficiency reported on the basis of direct-deposited CQD films, requiring no further treatment once dried. We propose that minimal amounts of unbound TG necessary in
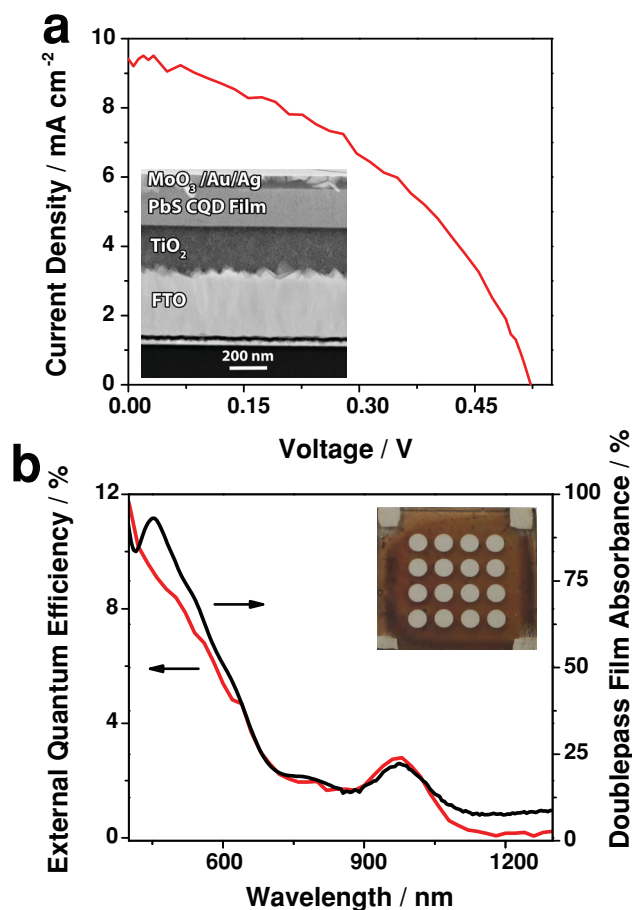
Figure 4. Characterization of proof-of-principle photovoltaic devices. a) Current–voltage characteristics leading to a photovoltaic performance of 2.1% PCE from our champion device with single-layer drop-cast TG-capped PbS CQD film with transmission electron microscopy image prepared by focussed ion beam milling displaying the layer structure of the p–n heterojunction device (inset a). b) Resulting external quantum efficiency spectrum and film absorbance spectrum emphasizing the preservation of quantum confinement after film formation of a very homogenous film (inset b).

solution to retain a stable, quantum-confined colloid are the cause for lower than expected device performance of the PbS CQD solar cells discussed in this manuscript, even though the average inter-particle distances remain similar (Figure S3, Supporting Information). A higher density of states than our previously published solar cells was extracted from Voc transient data of an average device (Figure S4, Supporting Information), indicating a connection between TG ligand remaining in the film, device performance and the lower-than-expected current density extracted from the EQE spectrum. Initial studies on solvent annealing of the device indicate that this technique might be helpful to address the present trap state density problem of the drop-casted CQD films. Our future work will discuss strategies on overcoming this limitation leading to increased device performance and improved density of states. The EQE spectrum and the film absorbance are in good agreement and demonstrate that we maintained quantum confinement in the CQD solid.

We sought to identify avenues to improved device performance on the basis of the single-step inks. We used TGA and XPS to compare the films derived from the directly deposited TG-capped CQDs and the highest-efficiency CQD devices reported to date on the basis of the layer-by-layer process.[5] We found total ligand coverage was around twice as low in the case of the ink-based films. This suggests that future work could investigate means to achieve complete ligand coverage with the goal of reducing the density of recombination centers.

These devices represent the first demonstration of a single-step solar cell fabrication process on the basis of PbS CQD inks. The solution exchange approach involving displacement to short, electronic-coupling-compatible ligands, with the resultant nanoparticles stabilized in a polar solvent, represents a promising step towards a manufacturable CQD solar technology. Its dramatic improvement in the efficiency of materials utilization paves the way to a cost-effective roll-to-roll technology

Experimental Section

Synthesis of PbS Quantum Dots: PbS colloidal quantum dots were synthesized using a variation on a literature method[29] reported in Tang et al.[27]

Solution-Phase Ligand Exchange Process: A two-phase exchange process was used to replace the OA synthesis ligands from the PbS CQDs (diluted to 4 mg mL^{-1}) with TG (21 mg mL^{-1} in DMSO) in a single step. The two phases were combined and vortexed vigorously for five seconds to form a microemulsion. After centrifugation for two minutes at ≈3200 rpm, the dark brown polar phase was separated from the clear non-polar phase. Octane was then added to the polar phase in a 1:1 ratio, followed by further vortexing and centrifugation to remove residual OA from the polar phase. This washing step was repeated four more times. After the final separation of the polar phase, ACN was added in a 1:1 ratio to induce precipitation of the TG-capped CQDs in the polar solution and centrifugation was used to isolate the precipitate. More ACN was added to the precipitate to remove any excess (unbound) TG. Finally, the TG-capped CQDs were dried in vacuum overnight to remove traces of ACN. DMSO was added to the precipitate and immediate redispersion of the TG-capped PbS CQDs was observed. A final centrifugation step at 13 krpm for five minutes was applied to ensure the removal of undissolved material. Typically, the CQD ink was diluted to a concentration of 50 mg ml^{-1} prior to film fabrication.

Formation of TG-Capped PbS CQD Films: Prior to film formation the TiO$_2$ electrode—deposited on FTO-coated glass[30]—was cleaned and its hydrophilicity and hence wettability increased via a 2-minute oxygen plasma treatment. 11 µL of the TG-capped PbS CQD solution at a concentration of 50 mg mL^{-1} were deposited on the substrates in an inert atmosphere. At room temperature, the films are completely dry after 6 hours; however, mild heating below 35 °C can be used to accelerate the drying process.

Optical Characterization: Linear optical absorption spectra were taken using a Cary UV-vis near-infrared (NIR) spectrometer (Varian). Glass cuvettes with a path length of 1 mm were used. For measurement purposes, the concentration of the CQD solution was adjusted to 0.4 mg/ml.

Photoluminescence Quantum Efficieny Measurements: PLQE measurements were performed at room temperature in air. A 640 nm diode laser with an intensity of approximately 10 W cm^{-2} was used as an excitation source. A NIR spectrometer with an InGaAs array detector (Ocean Optics NIR-512, calibrated using a tungsten halogen lamp as a known source) was connected through fiber optics with the integrating sphere where the sample was positioned. The laser light is directed to enter one of the two ports of the integrating sphere. The second port

is connected to an optical fiber to collect the spectra that are measured in direct and indirect excitation mode with the same NIR spectrometer. Low PbS CQD concentrations were used in these measurements to guarantee no reabsorption by the sample of the emitted PL signal. PLQE is calculated by taking the integrated difference between the directly excited and indirectly excited photoluminescence photon signals divided by the integrated difference between the direct-pump and indirect-pump laser photon signals.

Analytical ultracentrifugation: The AUC experiments were carried out with a Beckman Optima XL-A (controlled by a PC running Beckman Proteome Lab v 5.8 acquisition software) equipped with an An-60 Ti rotor and an optical absorbance detector, following a similar procedure as described in Harkness et al.[31–33] For the CQDs in DMSO, the concentration of the sample solutions (420 µL) was adjusted by diluting with DMSO until the optical absorbance at a wavelength of 273 nm was OD ≈ 1. The samples were then loaded into double-sector centerpieces with quartz windows. A reference neat DMSO solution was loaded in the sector adjacent to the sample solution. The samples were loaded in the rotor and left in the ultracentrifuge for about 5 hours until the temperature equilibrated at 20 °C. The ultracentrifuge was operated at a rotor speed of 16 000 rpm. To acquire sedimentation profiles, the sectors were scanned in 0.003 cm radial increments. The average time required to scan an entire sector was about 1 minute. We analyzed approximately 120 sedimentation profiles for the subtraction of time-invariant and radial-invariant noise, meniscus optimization, and Lamm equation modeling using Ultrascan III[31] two-dimensional spectrum analysis (2DSA).[32,33] Sedimentation–diffusion distributions were then obtained after Monte Carlo analysis (100 runs).[33] Solvent densities and viscosities were obtained from the USLIMS Database. For the CQDs in H$_2$O, the optical absorbance wavelength was chosen as 299 nm with OD about 0.8. The centrifuge speed was set to 6000 rpm, and 40 sedimentation profiles were used for analysis.

Diffusion-Ordered Spectroscopy: The DOSY NMR spectra were measured using the one-shot pulse sequence by Pelta.[20] Point-by-point analysis was done with two exponential functions to calculate the diffusion constants.[20,21] 1H and DOSY NMR spectra were recorded on an Agilent DD2 600 MHz spectrometer with an Agilent HFX indirect triple resonant probe. The "Doneshot" pulse sequence was used as supplied by Agilent. The gradient strengths were varied from 1.7 G cm^{-1} to 52 G cm^{-1} with a correction for non-uniform gradients. The diffusion delay was 250 ms, and 64 scans per gradient strength were collected.

Thermogravimetric Analysis: TGA of powder made from the CQD films was performed under N$_2$ flow with a ramp rate of 10 °C min^{-1} (TA Instrument SDT600 TGA/DSC, in platinum pans). After the film formation, the dried films were scratched off the substrates to obtain roughly 10 mg of material for the analysis.

Fourier Transform Infrared Spectroscopy: FTIR was performed on a Bruker Tensor spectrometer in transmission mode. KBr disks were used for all measurements. For the PbS CQD film fabrication, 10 µL of the CQD-DMSO solution were drop casted onto the KBr disks, and the sample was allowed to dry under inert conditions. For the reference measurement of 1-thioglycerol, 5 µL of the neat compound was drop-cast onto the disk, distributed over the entire disk as a thin film, and measured immediately afterwards. A background subtraction was performed for the entire data set.

Cross Polarization Magic Angle Spinning ^{13}C NMR: CP-MAS ^{13}C NMR measurements were collected on an Agilent DD2 700 MHz spectrometer with a 1.6 mm T2 NB HX Balun probe. The sample was rotated at a spinning speed of 10 kHz. A linearly ramped amplitude cross-polarization (CP) pulse sequence was used with a two-pulse phase-modulated decoupling method, which was provided by Agilent. A ^{1}H π/2 pulse width of 3.75 µs, Hartmann–Hahn matching condition of approximately 67 kHz, a contact time of 3.2 ms, and a recycle delay of 5.0 s were used. The spectral width was set to 48.1 kHz using 1024 complex points while 42 000 transients were collected. Chemical shifts were referenced to trimethyl silane (δ_{iso} = 0 ppm) using adamantane as a secondary reference (δ_{iso} = 38.3 ppm) for the high-frequency resonance.

X-ray Photoelectron Spectroscopy: XPS was measured with a Thermo Scientific K-Alpha spectrometer to confirm material composition before and after ligand exchange. A survey measurement was taken first, followed by recording the core level spectra of Pb-4f, S-2p, Cd-3d, Cl-2p, O-1s, and C-1s with a pass energy of 50 eV. The interpretation of the S-2p3/2 peak is described in detail in the manuscript. The binding energy was referenced to the C1s hydrocarbon line at 285.0 eV. The curves were fitted using Gaussian functions.

FIB-TEM: Samples made from TG-capped PbS ink were processed for cross-sectional TEM imaging. Zeiss NVision 40 focused ion beam (FIB) mill was used to prepare samples for TEM imaging. Thin films (of approximately 100 nm) were prepared with a Ga^+ beam followed by argon ion nano milling. A FEI Titan 80–300 Cubed STEM was used for imaging.

Photovoltaic Device Fabrication: PbS CQD films were deposited using the film formation process described in the main text. The top contacts were deposited in an angstrom engineering Å mod deposition system in an Innovative Technology glovebox. The contact procedure starts with 30 nm of thermally evaporated molybdenum trioxide deposited at a rate of 0.2 Å s^{-1}, followed by electron beam deposition of 50 nm of gold deposited at 1.5 Å s^{-1} and finishes with 120 nm of thermally evaporated silver deposited at 3.0 Å s^{-1}.

AM1.5 Photovoltaic Performance Characterization: Current–voltage data were measured using a Keithley 2400 source meter. The solar spectrum at AM1.5 was simulated to within class A specifications (less than 25% spectral mismatch) with a xenon lamp and filters (ScienceTech; measured intensity of 100 mW cm^{-2}). The source intensity was measured with a Melles–Griot broadband power meter through a circular 0.049 cm^2 aperture. We used the same aperture (shadow mask) in our *J–V* measurement, which is slightly smaller than the top electrode to avoid overestimating the photocurrent: the entire photon fluence passing through the aperture was counted as incident on the device for all analyses of JSC and EQE.[34] The spectral mismatch of the system was characterized using a calibrated reference solar cell (Newport). The total AM 1.5 spectral mismatch—taking into account the simulator spectrum and the spectral responsivities of the test cell, reference cell, and broadband power meter—was re-measured periodically and found to be ≈11%. This multiplicative factor, M = 0.89, was applied to the current density values of the *J–V* curve to most closely resemble true AM 1.5 performance.[35] The uncertainty of the current–voltage measurements was estimated to be 7%.

External Quantum Efficiency: EQE data were gathered by passing the output of a 400 W xenon lamp through a monochromator while applying appropriate order-sorting filters. The collimated output of the monochromator was measured through a 1 mm aperture with calibrated Newport 818-UV and Newport 818-IR power meters. The beam was optically chopped and co-focused on the pixel with a broadband solar simulator lamp source at approximately 1-sun intensity. A measurement bandwidth of ≈20 nm was used, and the intensity was varied according to the spectrum of the xenon lamp. A Stanford Research Systems lock-in amplifier operating in current mode detected the current response where a virtual null at the input approximated short-circuit conditions. The EQE spectra were measured at an estimated accuracy of ±8%.

Supporting Information

Supporting Information is available from the Wiley Online Library or from the author.

Acknowledgements

[1] M. De, P. S. Ghosh, V. M. Rotello, *Adv. Mater.* **2008**, *20*, 4225.

[2] M. A. Walling, J. A. Novakk, J. R. E. Shepard, *Int. J. Mol. Sci.* **2009**, *10*, 441.

[3] D. V. Talapin, J. S. Lee, M. V. Kovalenko, E. V. Shevchenko, *Chem. Rev.* **2010**, *110*, 389.

[4] E. H. Sargent, *Nat. Photonics*, **2009**, *6*, 133.

[5] D. B. Mitzi, M. Yuana, W. Liua, A. J. Kellock, S. J. Cheya, L. Gignac, A. G. Schrott, *Thin Solid Films*, **2009**, *517*, 2158.

[6] Q. Guo, G. M. Ford, R. Agrawal, H. W. Hillhouse, *Prog. Photovolt. Res. Appl.*, **2013**, *21*, 64.

[7] Q. Guo, G. M. Ford, W.-C. Yang, B. C. Walker, E. A. Stach, H. W. Hillhouse, R. Agrawal, *J. Am. Chem. Soc.*, **2010**, *132*, 17384.

[8] G. M. Ford, Q. Guo, R. Agrawal, H. W. Hillhouse, *Chem. Mater.*, **2011**, *23*, 2626.

[9] A. H. Ip, S. M. Thon, S. Hoogland, O. Voznyy, D. Zhitomirsky, R. Debnath, L. Levina, L. R. Rollny, G. H. Carey, A. Fischer, K. W. Kemp, I. J. Kramer, Z. Ning, A. J. Labelle, K. W. Chou, A. Amassian, E. H. Sargent, *Nat. Nanotechnol.* **2012**, *7*, 577.

[10] X. Lan, J. Bai, S. Masala, S. M. Thon, Y. Ren, I. J. Kramer, S. Hoogland, A. Simchi, G. I. Koleilat, D. Paz-Soldan, Z. Ning, A. J. Labelle, J. Y. Kim, G. Jabbour, E. H. Sargent, *Adv. Mater.* **2013**, *25*, 1769.

[11] Z. Ning, D. Zhitomirsky, V. Adinolfi, B. Sutherland, J. Xu, O. Voznyy, P. Maraghechi, X. Lan, S. Hoogland, Y. Ren, E. H. Sargent, *Adv. Mater.* **2013**, *25*, 1719.

[12] Y. Zhang, A. Clapp, *Sensors* **2011**, *11*, 11036.

[13] B. Xue, J. Cao, D. Deng, J. Xia, J. Jin, Z. Qian, Y. Gu, *J. Mater. Sci. Mater. Med.* **2012**, *23*, 723.

[14] D. Deng, W. Zhang, X. Chen, F. Liu, J. Zhang, Y. Gu, J. Hong, *Eur. J. Inorg. Chem.* **2009**, 3440.

[15] X.-S. Zhao, S.-Y. Xu, L.-Y. Liang, T. Li, S. Cauchi, *J. Mater. Sci.* **2007**, *42*, 4265.

[16] Y. Yu, K. Zhang, S. Sun, *Appl. Surf. Sci.* **2012**, *258*, 7181.

[17] L. Bakueva, I. Gorelikov, S. Musikhin, X. S. Zhao, E. H. Sargent, E. Kumacheva, *Adv. Mater.* **2004**, *16*, 926.

[18] G. Konstantatos, L. Levina, A. Fischer, E. H. Sargent, *Nano Lett.* **2008**, *8*, 1446.

[19] K. L. Planken, H. Cölfen, *Nanoscale* **2010**, *2*, 1849.

[20] M. D. Pelta, G. A. Morris, M. J. Tschedroff, S. J. Hammond, *Magn. Reson. Chem.* **2002**, *40*, 147.

[21] B. Fritzinger, R. K. Capek, K. Lambert, J. C. Martins, Z. Hens, *J. Am. Chem. Soc.* **2010**, *132*, 10195.

[22] R. Gomes, A. Hassinen, A. Szczygiel, Q. Zhao, A. Vantomme, J. C. Martins, Z. Hens, *J. Phys. Chem. Lett.* **2011**, *2*, 145.

[23] H. Ko, G. Shim, Y. Kim, *Bull. Korean Chem. Soc.* **2005**, *26*, 2001.

[24] D. I. Kim, M. A. Islam, L. Avila, I. P. Herman, *J. Phys. Chem. B* **2003**, *107*, 6318.

[25] A. Aboulaich, L. Balan, J. Ghanbaja, G. Medjahdi, C. Merlin, R. Schneider, *Chem. Mater.* **2011**, *23*, 3706.

[26] D. H. Lee, R.A. Condrate Sr., *J. Mater. Sci.* **1999**, *34*, 139.

[27] J. Tang, L. Brzozowski, D. A. R. Barkhouse, X. Wang, R. Debnath, R. Wolowiec, E. Palmiano, L. Levina, A. G. Pattantyus-Abraham, D. Jamakosmanovic, E. H. Sargent, *ACS Nano* **2010**, *4*, 869.

[28] A.G. Pattantyus-Abraham, I. J. Kramer, A. R. Barkhouse, X. Wang, G. Konstantatos, R. Debnath, L. Levina, I. Raabe, M. K. Nazeeruddin, M. Graetzel, E. H. Sargent, *ACS Nano* **2010**, *4*, 3374.

[29] M. A. Hines, G. D. Scholes, *Adv. Mater.* **2003**, *15*, 1844.

[30] H. Liu, J. Tang, I. J. Kramer, R. Debnath, G. I. Koleilat, X. Wang, A. Fisher, R. Li, L. Brzozowski, L. Levina, E. H. Sargent, *Adv. Mater.* **2011**, *23*, 3832.

[31] K. M. Harkness, Y. Tang, A. Dass, J. Pan, N. Kothalawala, V. J. Reddy, D. E. Cliffel, B. Demeler, F. Stellacci, O. M. Bakr, J. A. McLean, *Nanoscale*, **2012**, *4*, 4269.

[32] E. Brookes, W. M. Cao, B. Demeler, *Eur. Biophys. J.*, **2010**, *39*, 405.

[33] B. Demeler, E. Brookes, *Colloid Polym. Sci.* **2008**, *286*, 129.

[34] H. J. Snaith, *Nat. Photonics* **2012**, *6*, 337.

[35] J. M. Kroon, M. M. Wienk, W. J. H. Verhees, J. C. Hummelen, *Thin Solid Films* **2002**, *403*, 223.